

Correlated physics, charge and magnetic orders in moiré kagomé systems

Zhaochen Liu(刘兆晨) and Jing Wang(王靖)

Citation: Chin. Phys. B, 2025, 34 (**2**): 027304. DOI: 10.1088/1674-1056/ad9ffa
Journal homepage: http://cpb.iphy.ac.cn; http://iopscience.iop.org/cpb

What follows is a list of articles you may be interested in

Higher-order topological corner states and origin in monolayer LaBrO

Qing Wang(王庆) and Ning Hao(郝宁)
Chin. Phys. B, 2024, 33 (**12**): 127303. DOI: 10.1088/1674-1056/ad8a50

Perspectives of spin-valley locking devices

Lingling Tao(陶玲玲)
Chin. Phys. B, 2023, 32 (**10**): 107306. DOI: 10.1088/1674-1056/acc809

Two-dimensional tetragonal ZnB: A nodalline semimetal with good transport properties

Yong-Chun Zhao(赵永春), Ming-Xin Zhu(朱铭鑫), Sheng-Shi Li(李胜世), and Ping Li(李萍)
Chin. Phys. B, 2023, 32 (**6**): 067301. DOI: 10.1088/1674-1056/ac8f33

Recent advances of defect-induced spin and valley polarized states in graphene

Yu Zhang(张钰), Liangguang Jia(贾亮广), Yaoyao Chen(陈瑶瑶), Lin He(何林), and Yeliang Wang(王业亮)
Chin. Phys. B, 2022, 31 (**8**): 087301. DOI: 10.1088/1674-1056/ac70c4

Floquet topological phase transition in two-dimensional quadratic band crossing system

Guo-Bao Zhu(朱国宝) and Hui-Min Yang(杨慧敏)
Chin. Phys. B, 2021, 30 (**6**): 067304. DOI: 10.1088/1674-1056/abdda4

SPECIAL TOPIC — Moiré physics in two-dimensional materials

Correlated physics, charge and magnetic orders in moiré kagomé systems

Zhaochen Liu(刘兆晨)[1,2] and Jing Wang(王靖)[1,2,3,4,†]

[1] *State Key Laboratory of Surface Physics and Department of Physics, Fudan University, Shanghai* 200433, *China*
[2] *Shanghai Research Center for Quantum Sciences, Shanghai* 201315, *China*
[3] *Institute for Nanoelectronic Devices and Quantum Computing, Fudan University, Shanghai* 200433, *China*
[4] *Hefei National Laboratory, Hefei* 230088, *China*

(Received 21 October 2024; revised manuscript received 29 November 2024; accepted manuscript online 17 December 2024)

Moiré systems have emerged as an ideal platform for exploring interaction effects and correlated states. However, most of the experimental systems are based on either triangular or honeycomb lattices. In this study, based on the self-consistent Hartree–Fock calculation, we investigate the phase diagram of the kagomé lattice in a recently discovered system with two degenerate Γ valley orbitals and strong spin–orbit coupling. By focusing on the filling factors of $1/2$, $1/3$ and $2/3$, we identify various symmetry-breaking states by adjusting the screening length and dielectric constant. At the half filling, we discover that the spin–orbit coupling induces Dzyaloshinskii–Moriya interaction and stabilizes a classical magnetic state with 120° ordering. Additionally, we observe a transition to a ferromagnetic state with out-of-plane ordering. In the case of $1/3$ filling, the system is ferromagnetically ordered due to the lattice frustration. Furthermore, for $2/3$ filling, the system exhibits a pinned droplet state and a 120° magnetic ordered state at weak and immediate coupling strengths, respectively. For the strong coupling case, when dealing with non-integer filling, the system is always charge ordered with sublattice polarization. Our study serves as a starting point for exploring the effects of correlation in moiré kagomé systems.

Keywords: moiré kagomé system, Hartree–Fock, spin–orbit coupling

PACS: 73.20.–r, 73.43.Cd, 71.70.Ej, 68.65.–k

DOI: 10.1088/1674-1056/ad9ffa **CSTR:** 32038.14.CPB.ad9ffa

1. Introduction

The recent advances in van der Waals moiré systems have opened up a new direction in condensed matter physics.[1–5] Inspired by the discovery of correlated states and superconductivity in twisted bilayer graphene,[6,7] a variety of phenomena have been explored both experimentally and theoretically over the past several years.[6–13] Besides the graphene system, the Mott–Wigner insulator, quantum criticality and the fractional Chern insulator have been found in transition metal dichalocogenide (TMD) superlattices.[14–29] In these systems, the electrons are confined by the interface moiré potential, resulting in miniband structures with different effective lattices.[8,30–35] The enlarged moiré unit cell reduces the kinetic energy, so strong electron interactions can dominate.[36–52] The flexibility and rich choice of two-dimensional materials provide an ideal platform for quantum simulators in solid-state systems.

However, the experimental systems in moiré TMD superlattices have only triangular or honeycomb lattice structures. On the other hand, previous studies have found hierarchical lattice structures, including a honeycomb lattice followed by a kagomé lattice in the single orbital Γ-valley moiré TMD and magnetic moiré surface state of topological insulators.[32,33,53]

The kagomé lattice, which is located at higher energy bands, only emerges at small twisting angles. This hinders its experimental accessibility. To address this challenge, two-orbital Γ valley moiré systems were proposed.[54,55] It was found that the additional orbital degree of freedom facilitates the manifestation of the kagomé band structure near the charge neutral point. However, one may also realize a kagomé lattice by the interaction effect in a single-orbital moiré system[42] and in Kekulé graphene.[56,57]

Here we explore the interaction phase diagrams of the kagomé lattice in moiré systems, motivated by recent advancements in their realization. The kagomé lattice is an ideal platform for studying the strong correlation effect, as its lattice structure is fully frustrated.[58,59] The Hubbard model has been used to study various phenomena, such as the Mott transition,[60–63] ferromagnetism,[64–68] density waves,[69–75] topology[70,76–78] and exotic superconductivity induced by the van Hove singularity.[79–83] At half filling and the strong interaction limit, the kagomé lattice Heisenberg model is known as a representative system for quantum spin liquids.[84–90] Spin–orbit coupling (SOC) induces the Dzyaloshinskii–Moriya (DM) interaction and stabilizes the classical magnetic order state.[91–94] A t–J model with a finite dopant has also been

†Corresponding author. E-mail: wjingphys@fudan.edu.cn

© 2025 Chinese Physical Society and IOP Publishing Ltd. All rights, including for text and data mining, AI training, and similar technologies, are reserved.

studied.[65,95–101] Therefore, to better understand our system, we have studied the effect of interactions through the Hartree–Fock (HF) method.

The organization of this paper is as follows. In Section 2, we describe the Hamiltonian and the symmetries of the system, and the Wannier function is constructed by using the selected columns of the density matrix method.[102–104] Then, HF Hamiltonian is obtained by projecting the Coulomb interaction onto the kagomé bands in the Wannier basis. In Section 3, we present the HF results on the $1/2$, $1/3$ and $2/3$ fillings. Section 4 concludes the paper with discussions.

2. Model

2.1. Hamiltonian

We first review the model for a twisted multi-orbital bilayer. Different from a TMD system like $MoTe_2$,[30] the system we considered has low-energy physics consisting of two degenerate valance bands at the Γ point.[54,55] The generic moiré Hamiltonian can be obtained in analogy to the Bistritzer–MacDonald model for TBG as[8,54]

$$H_{\text{bilayer}} = \begin{pmatrix} H_0 & V(\boldsymbol{r}) \\ V^\dagger(\boldsymbol{r}) & H_0 \end{pmatrix}, \tag{1}$$

where H_0 is the kinetic energy of the single-layer part, and $V(\boldsymbol{r})$ is the moiré potential represented by position-dependent interlayer tunneling. For the single layer part, on the basis of angular momentum $l_z = \mp 1$ and C_{6v} symmetry, we have

$$\begin{aligned} H_0 = & -\frac{\hbar^2}{2m}\{(k_x^2+k_y^2)+\kappa[(k_x^2-k_y^2)\tau_x+2k_xk_y\tau_y]\} \\ & +\frac{\lambda_s}{2}\tau_z\sigma_z, \end{aligned} \tag{2}$$

where τ_i and σ_i $(i = x, y, z)$ are Pauli matrices for orbital and spin degrees, m is the average effective mass, λ_s is the SOC strength, and $\kappa = (m_+ - m_-)/(m_+ + m_-)$ represents the effective mass ratio of the heavy (m_+) and light (m_-) holes. The moiré potential can be expanded as

$$V(\boldsymbol{r}) = V_0 + \sum_{n,i=1}^{6} V_{n,i}\, e^{i\boldsymbol{g}_{n,i}\cdot\boldsymbol{r}}, \tag{3}$$

with $g_{n,i}$ as moiré reciprocal vectors related by C_6 rotation and $g_{n,1} = -g_{n,4}$, $g_{n,2} = -g_{n,5}$, $g_{n,3} = -g_{n,6}$. Moreover, the C_{6v} and time-reversal symmetry constrains the matrix V_{g_i} as

$$\begin{aligned} V_{n,1} &= \begin{pmatrix} \alpha_n & \beta_n e^{-i\frac{\pi}{3}} \\ \beta_n e^{i\frac{\pi}{3}} & \alpha_n \end{pmatrix}, \quad V_2 = \begin{pmatrix} \alpha_n & -\beta_n \\ -\beta_n & \alpha_n \end{pmatrix}, \\ V_3 &= \begin{pmatrix} \alpha_n & \beta_n e^{i\frac{\pi}{3}} \\ \beta_n e^{-i\frac{\pi}{3}} & \alpha_n \end{pmatrix}. \end{aligned} \tag{4}$$

The moiré potential can trap particles in either triangular, honeycomb or even kagomé lattices depending on the parameters.[54] The trapped particles would naturally form different orbitals inside such moiré atoms. For a single-band system such as MoS_2,[32,33] these orbitals show conventional hierarchies. The s-orbital has the lowest energy, followed by the p-orbital and d-orbital. However, for the two-band system considered here, the moiré potential couples non-trivially on different bands. Therefore, it is possible to arrange the orbital sequences. For example, our previous work showed that twisted bilayer CdS exhibits a band structure with two degenerate p_x, p_y orbitals on the honeycomb lattice and PdS_2 has a kagomé lattice band structure[54] (similar kagomé physics also apply to ZrS_2[55]). In this paper, we focus on the PdS_2 with the parameters $V_0 = 0$, $\alpha_1 = -24.3$ meV, $\alpha_2 = 5.5$ meV, $\beta_1 = 26.8$ meV, and $\beta_2 = 10.3$ meV. For the single-layer part, $0.7m_e$ with m_e as the mass of free electron, $\kappa = 0.9$ and $\lambda_s = 65$ meV. In the following, to simplify the analysis, we also add particle–hole transformation to our system. The corresponding moiré pattern and band structure are shown in Figs. 1(a) and 1(b), respectively. Furthermore, we focused on twisting angles ranging from 1.5° to 3.5°, ensuring that the low-energy subspace remains well-separated from remote bands.[54]

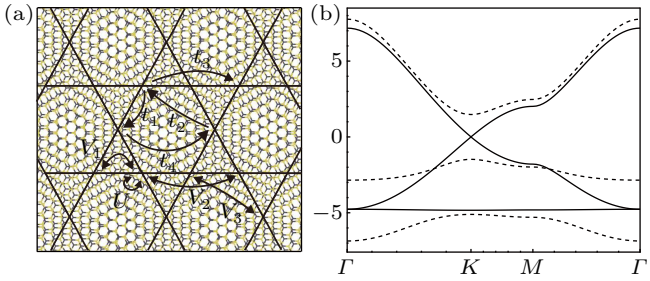


Fig. 1. (a) The moiré lattice of twisted bilayer PdS_2. The solid lines represent the kagomé lattice. (b) The solid and dashed lines show the band structure at twisting angle $\theta = 2.5^\circ$, with and without SOC, respectively. We have shifted the Dirac point to the zero energy.

2.2. Wannier function

Since our target is to study symmetry-breaking states with different magnetic and charge order through the HF method. The self-consistent calculation depends on the initial ansatz. Therefore, in order to have a better controllability of the HF calculation, we first construct the Wannier state of the moiré bands. We then project the Coulomb interaction onto them.

Given the Bloch wave function $\psi_{n,\boldsymbol{k},\sigma}(\boldsymbol{r})$ with energy $\varepsilon_n(\boldsymbol{k})$ where n is the band index and σ is the spin index. The Wannier function in the unit cell $\boldsymbol{R}$ is constructed from a Fourier transformation as[105]

$$w_{n,\sigma}(\boldsymbol{r}-\boldsymbol{R}) = \frac{1}{N}\sum_{k} e^{i\boldsymbol{k}\cdot\boldsymbol{R}}\psi_{n,\boldsymbol{k},\sigma}(\boldsymbol{r}), \tag{5}$$

where N is the number of momentum points. However, there is additional "gauge redundancy" in the definition of the Wannier function. The unitary transformations within the given set

of bands also provide possible realizations

$$\psi_{n,\boldsymbol{k},\sigma}(\boldsymbol{r}) \to \sum_m \psi_{m,\boldsymbol{k},\sigma}(\boldsymbol{r})[U_\sigma(\boldsymbol{k})]_{m,n}. \tag{6}$$

To fix this issue, Marzari and Vanderbilt proposed that $U_\sigma(\boldsymbol{k})$ could be obtained by minimizing the spreading functional.[105] This method has been widely used to construct Wannier states in moiré systems with a physically inspired initial state.[106–109] One drawback is that it requires appropriate initial guesses. However, in our system, the four-component wave function complicates the initial guess. Therefore, we approach this problem by using the recently proposed selected columns of the density matrix (SCDM) method.[102–104] The SCDM, as a parameter-free method for isolated band structures, can automatically generate the transformation matrices. The robustness of the SCDM has been well tested in first-principles material calculations.[110]

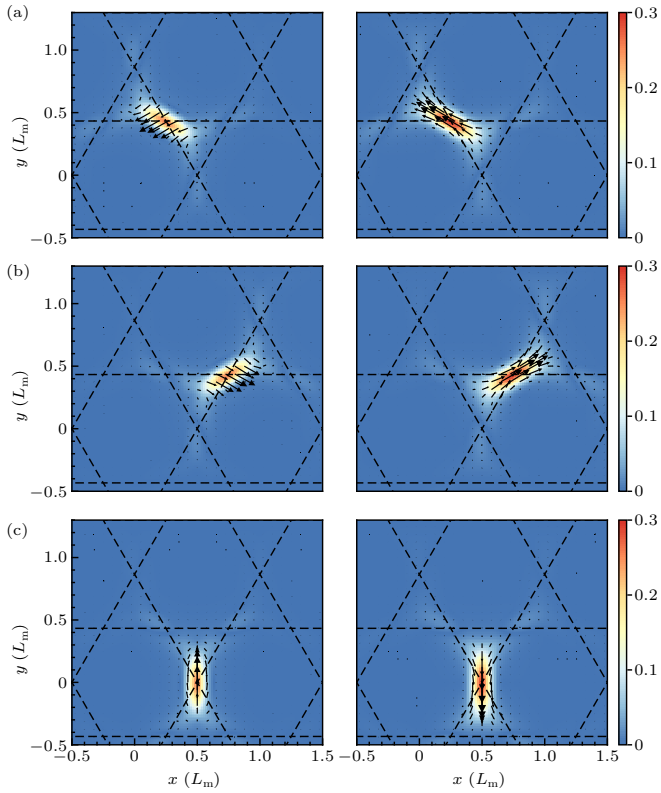


Fig. 2. (a)–(c) The amplitude of the Wannier function for two orbitals of the top layer for three sublattices. The arrows represent the phase of the wave function.

Figure 2 shows the density distribution of the Wannier state for a spin-up particle. As we can see, the Wannier state is well localized and located precisely at the kagomé lattice. We also applied the Marzari–Vanderbilet method to optimize it, but it did not show any improvement. Moreover, in our case, we find the density distribution fulfills the symmetry requirement. We should note that the additional global phases of the three sublattices have not yet been determined.[108] To fix the global gauge, we first set the first component of the Wannier function to be real and positive at the kagomé triangle center. Then, we apply additional phase factor $\exp[-\mathrm{i}(\frac{2\pi}{3}j+\frac{\pi}{6})]$ for $j=1,2,3$ labels of three sublattices. The arrows in Fig. 2 show the phase of the wave function. From which, we find, under C_3 rotation, that the Wannier function transforms as

$$w_{n,\sigma}(\boldsymbol{r}) = \mathrm{e}^{-\frac{2\pi}{3}\tau_z} w_{C_3^{-1}n,\sigma}(R_3^{-1}\boldsymbol{r}), \tag{7}$$

where we have set the coordinate origin at the kagomé triangular center. We can check that the constructed Wannier states are consistent with the symmetries in our system. The Wannier states for spin-down were obtained in the same way.

After construction of the $U_\sigma(\boldsymbol{k})$, the Hamiltonian on the basis of Wannier states is given by

$$\tilde{H}_{0,\sigma}(\boldsymbol{k}) = U_\sigma^\dagger(\boldsymbol{k})\epsilon(\boldsymbol{k},\sigma)U_\sigma(\boldsymbol{k}), \tag{8}$$

and the real-space tight-binding Hamiltonian is

$$H = \sum_{i,j} c_{i,\sigma}^\dagger h_{i,j}^\sigma c_{j,\sigma}, \tag{9}$$

where i, j refer to a different unit cell and

$$h_{i,j}^\sigma = \frac{1}{N}\sum_{\boldsymbol{k}} \mathrm{e}^{\mathrm{i}\boldsymbol{k}\cdot(\boldsymbol{R}_i-\boldsymbol{R}_j)}\tilde{H}_{0,\sigma}(\boldsymbol{k}), \tag{10}$$

from which we can read out the hopping strength between different sites. The hopping strengths up to third-nearest neighbor are shown in Fig. 3(a). The SOC introduces phases in nearest t_1 and next-nearest hopping t_2. Meanwhile, due to the inversion symmetry, the t_3 and t_4 are real. Furthermore, we find that the amplitude of t_2 and t_3 are comparable and t_4 is much smaller. This behavior could be understood from the shape of the Wannier state. The Wannier state consists of two parts, trunks and branches. Four branches actually extend to nearby triangles. Therefore, for t_2 and t_3 terms, the trunk of one site overlaps with the branch of another site. However, for a t_4 process, two Wannier states only overlap at the branch part. Accordingly, we have $|t_1| \gg |t_2| \simeq |t_3| \gg |t_4|$. Additionally, the real part of t_1 is positive, which indicates that the flat band is located at the bottom rather than at the top, as in conventional kagomé models.

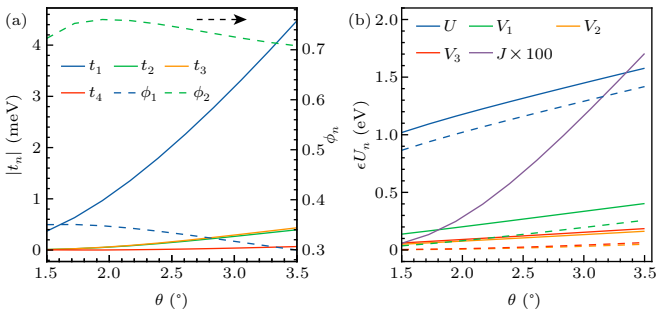


Fig. 3. (a) The hopping strengths (solid lines) $|t_n|$ and the SOC phase (dashed lines) ϕ_n as a function of twisting angle θ. (b) The interaction parameter ϵU_n at screening length $d_\mathrm{s} = 30$ nm (solid lines) and $d_\mathrm{s} = 10$ nm (dashed lines), respectively.

2.3. Interaction Hamiltonian and HF method

In this section, we provide our formula for the self-consistent HF method. The bare Coulomb interaction Hamiltonian is

$$H_{\text{int}} = \frac{1}{2A}\sum_{\boldsymbol{q},\boldsymbol{k},\boldsymbol{k}',\sigma,\sigma',\alpha,\beta} V(\boldsymbol{q}) c^{\dagger}_{\alpha,\boldsymbol{k}+\boldsymbol{q}} c^{\dagger}_{\beta,\boldsymbol{k}'-\boldsymbol{q}} c_{\beta,\boldsymbol{k}'} c_{\alpha,\boldsymbol{k}}, \quad (11)$$

where the momentum summation is over all the momentum points and α,β are indices including orbital, layer and spin degrees of freedoms. Following previous treatments in moiré systems, we project the interaction onto the Wannier state in momentum space as[111–113]

$$\begin{aligned} H_{\text{int}} = & \frac{1}{2A}\sum_{\boldsymbol{G},\boldsymbol{q},\boldsymbol{k},\boldsymbol{k}',n_i} V(\boldsymbol{q}+\boldsymbol{G})\langle n_1,\boldsymbol{k}+\boldsymbol{q}+\boldsymbol{G}|n_4,\boldsymbol{k}\rangle \\ & \times\langle n_2,\boldsymbol{k}'|n_3,\boldsymbol{k}'+\boldsymbol{q}+\boldsymbol{G}\rangle \\ & \times c^{\dagger}_{n_1,\boldsymbol{k}+\boldsymbol{q}} c^{\dagger}_{n_2,\boldsymbol{k}'-\boldsymbol{q}} c_{n_3,\boldsymbol{k}'} c_{n_4,\boldsymbol{k}}, \end{aligned} \quad (12)$$

where summation for $\boldsymbol{G}$ is over all the reciprocal lattices and $\boldsymbol{k},\boldsymbol{k}'$ and $\boldsymbol{q}$ are restricted inside the first moiré Brillioun zone. $c_{n_i,\boldsymbol{k}}$ are the annihilation operator for Wannier states $n_i = 1,2,3$. The wave functions $|n_i,\boldsymbol{k}\rangle$ were obtained by the unitary transformation mentioned in the previous section. In the derivation of the above formula, we have explicitly assumed the periodic gauge, i.e., $c_{n,\boldsymbol{k}+\boldsymbol{G}} = c_{n,\boldsymbol{k}}$. Then, the HF decomposition is performed as usual and we allow the translation and spin $U(1)$ symmetries to be broken. The dual-gate screened Coulomb potential $V(\boldsymbol{q}) = (e^2/(2\epsilon\epsilon_0 q))\tanh qd_{\text{s}}$ was used. The dielectric constant ϵ is determined by the substrate and the screening length d_{s} is the gate–sample distance. Those two parameters will be used as tuning parameters together with the twisting angle θ to explore the phase diagrams. The self-consistent results crucially depend on the initial order parameter $\langle c^{\dagger}(\boldsymbol{k}')c(\boldsymbol{k})\rangle$; we initialize the order parameter with certain magnetic and charge order and iteratively update the order parameter until convergence. To accelerate this self-consistent calculation, we use the EDIIS + DIIS method with subspace size from 4 to 10.[114,115] A finite temperature with $T = 50$ mK is used to ensure numerical stability. The filling factor is defined as $\nu = N_{\text{p}}/(6N)$, where N_{p} is the particle number and N is the number of momentum points. In the following, the HF calculations are performed on a 12×12 momentum lattice.

On the other hand, one may project the interaction onto the Wannier state in real space to obtain the strength of relevant terms and gain a better understanding of the system.[39,40,45,109] In Fig. 3(b), we show the parameters for density–density interactions and nearest-neighbor ferromagnetic (FM) direct exchanges. Comparing with the single-particle hopping strength, we find the Hubbard interaction $\epsilon U/|t_1|$ ranges from 2500 at $\theta = 1.5^{\circ}$ to 370 at $\theta = 3.5^{\circ}$ for screening length $d_{\text{s}} = 30$ nm. The nearest V_1 is roughly three times smaller than Hubbard U. The V_2 and V_3 have comparable strength. Moreover, the direct FM exchange coupling, ϵJ_{d}, is around a few tens of meV. As we will show below, the direct exchange coupling plays a crucial role under certain parameters. Furthermore, we emphasize that the full Hamiltonian, Eq. (12), is used in our HF calculation, rather than a real-space Hubbard model.

3. Results

3.1. The half filling

At half filling and in the strong coupling limit, the electrons form local magnetic moments that are coupled with each other through the Heisenberg interaction. The isotropic kagomé Heisenberg antiferromagnet has long been proposed as an ideal platform for quantum spin liquids. However, for our system, due to the SOC, the spin Hamiltonian is actually described by the XXZ model with the DM interactions as[38,49]

$$H_{\text{s}} = J\sum_{\langle i,j\rangle} J^z_i J^z_j + \cos 2\phi_{i,j}\boldsymbol{S}^{\parallel}\cdot\boldsymbol{S}^{\parallel} + \sin 2\phi_{i,j}(\boldsymbol{S}_i\times\boldsymbol{S}_j), \quad (13)$$

where the phase variable $\phi_{i,j}$ is the same as the single-particle hopping one. We have omitted the long-ranged term as the corresponding hopping terms are one order of magnitude smaller than the nearest one. Moreover, including only the Hubbard U and nearest V_1, we can estimate $J = 4|t_1|^2/(U - V_1)$.[116] Since the DM interaction would induce classical magnetic order out of the quantum spin liquid.[91–94] We only consider regular magnetic orders identified previously.[94]

The HF energy for various magnetic orders is shown in Figs. 4(a) and 4(b) for $\theta = 2^{\circ}$ without and with spin–orbit coupling for different dielectric constant ϵ. As we expected, multiple states are almost degenerate with each other for large ϵ when the SOC is absent. By comparing the energy of different magnetic orders with previously obtained energy values from the classical Heisenberg model,[94] we can conclude that our system at $\theta = 2^{\circ}$ is dominated by nearest-neighbor Heisenberg coupling with weakly extended ones. After decreasing the ϵ, there is a first-order phase transition to the FM order. A decreased ϵ leads to a stronger Hubbard interaction and a weakened antiferromagnetic (AFM) coupling. However, the FM direct exchange is inversely proportional to the ϵ. Such competition between direct exchange and superexchange leads to this phase transition.[45]

After including the SOC, the anisotropic term and DM interaction break the degeneracy within the group of states. In addition, the $Q = 0_2$ state, 120° AFM order with opposite chirality between the spin and the real space, was selected as ground state in the AFM region. Moreover, the energy for the $\theta = 1.5^{\circ}$ case is shown in Fig. 4(c). Different twisting angles introduce only quantitative changes in the phase diagram. However, by closely comparing the results for $\theta = 2^{\circ}$ and

1.5°, we found that all the magnetic ordered states had almost the same energy at the transition point, which indicates full compensation between the FM and the AFM couplings. The nearby metallic gate can only reduce the long-range interaction such that the phase boundary only shifts slightly towards the smaller ϵ side when the screening length d_s is shorter than the moiré lattice constant. We notice that the HF results for the magnetic order are essentially classical; it would be interesting to study the effect of quantum fluctuation with more sophisticated methods in the future.

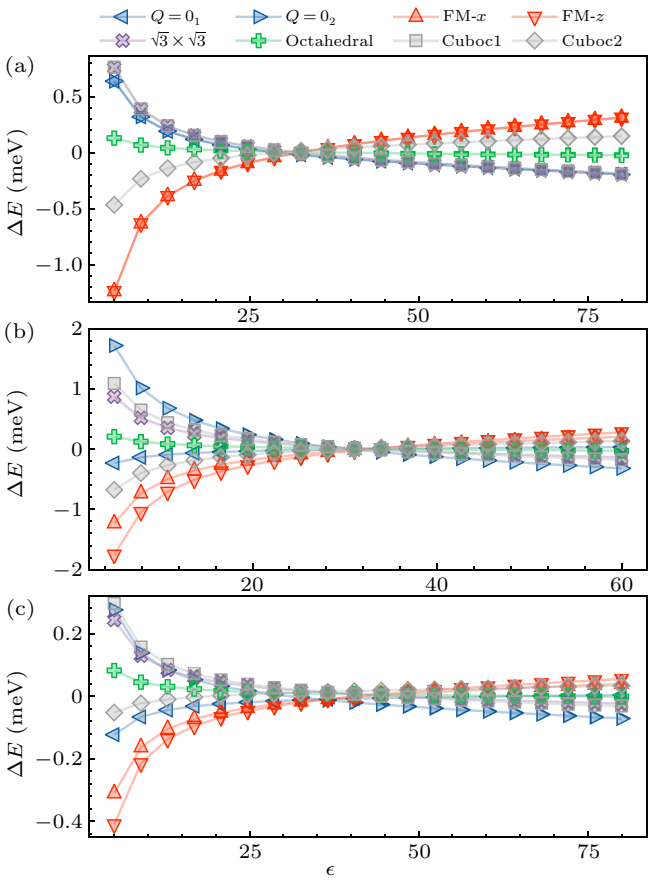


Fig. 4. The ground-state energy per original unit cell for various magnetic orders as a function of dielectric constant ϵ. All the energies are measured by the average energy. [(a) and (b)] The results for twisting angle $\theta = 2°$ without and with SOC, respectively. (c) The result for $\theta = 1.5°$. The gate screening distance is chosen as $d_s = 30$ nm. The octahedral and cuboc states are described with magnetic moments pointing to the vertices of the octahedron and cuboctahedron,[94] respectively.

3.2. The 1/3 filling

For the $1/3$ filling, i.e., two electrons per unit cell, the phase diagram is shown in Fig. 5(a) for $\theta = 2°$. For longer screening length, i.e., $d_s \gtrsim 8$ nm, the system exhibits out-of-plane FM order with a charge density wave (CDW) when $\epsilon \lesssim 20$. Then, with increased ϵ, there is a first-order phase transition to the FM-z state. Furthermore, the system transforms to the in-plane FM order FM-x by a first order transition near $\epsilon = 80$. We also show the phase diagram in the $\theta - \epsilon$ plane with $d_s = 30$ nm in Fig. 5(b).

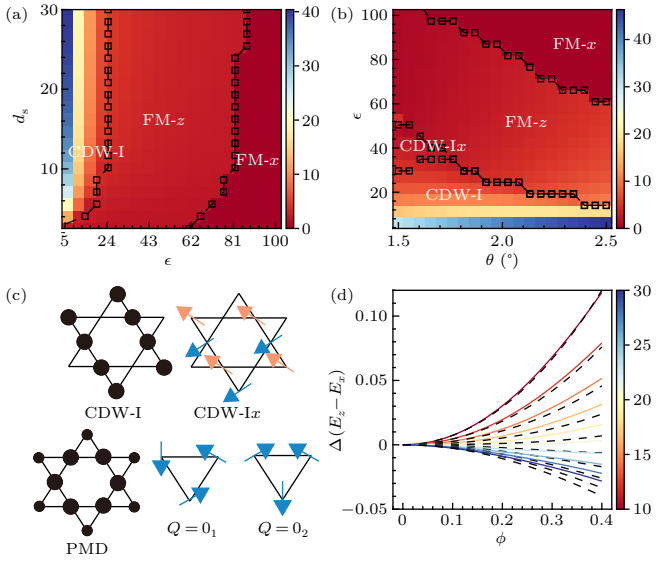


Fig. 5. [(a) and (b)] The phase diagram at filling $1/3$ in the d_s–ϵ and ϵ–θ planes, respectively. The color represents the band gaps. The FM-x state is nearly gapless, while the size of the gap in the FM-z state is determined by the SOC strength. (c) The pattern of possible charge density wave (CDW) states. In our system, the CDW-I state is the most stable and CDW-I-x with an in-plane magnetic order only appears at a small twisting angle with moderate interaction. (d) The energy difference between the FM-z state and the FM-x state is depicted as a function of the SOC strength for various Hubbard U in the lattice model. The color shows the strength of the Hubbard U and we have assumed a fully polarized magnetic order. The dashed lines represent the analytical results.

3.2.1. FM order

To understand the phase diagram, we notice the interaction strength is about $\epsilon U/|t_1| \sim 1200$, $\epsilon V_1/|t_1| \sim 210$ and $\epsilon V_2/|t_1| \approx \epsilon V_3/|t_1| \sim 85$ for $d_s = 30$ nm. Therefore, inside the FM phase, only the on-site Hubbard U is at the strong coupling limit especially for $\epsilon \sim 80$. In addition, the ferromagnetic order also appears at the extreme limit of screening with $d_s = 1$ nm. Therefore, the extended V term is not crucial for understanding the FM phases. Thus, the minimal model would be the Hubbard model as

$$H_{t-J} = |t_1| \sum_{i,j,\sigma} \mathrm{e}^{\mathrm{i}\sigma\phi_{i,j}} c^{\dagger}_{i,\sigma} c_{j,\sigma} + \sum U n_{i,\uparrow} n_{i,\downarrow}. \tag{14}$$

Without SOC, i.e., $\phi_{i,j} = 0$, the strong coupling of this model, namely, the t–J model, has been studied before in that the FM state is the ground state for a large range of exchange coupling $J/|t_1|$ for hole doping.[65,66] One may understand this from Nagaoka's ferromagnetism,[117,118] as when $J = 0$, the positive sign of single-particle hopping term fulfills the requirement of Nagaoka's theorem. However, as Nagaoka's ferromagnetism only applies to the single-hole case, the frustrated lattice structure would still lead to the FM order. For example, the ferromagnetism in a triangular lattice was also discussed recently.[119–123] Moreover, for our system, the FM direct exchange term would overcome the AFM superexchange at the $\epsilon \to 0$ limit.

To account for the SOC, the corresponding t–J model has not been investigated before. For the strong coupling limit,

namely, $J \to 0$, we could still anticipate the FM-z state, at least for the weak SOC. To have a better understanding of the role of the SOC, we decompose the Hubbard term by assuming a fully polarized magnetic order as

$$U n_{i,\uparrow} n_{i,\downarrow} \to -2U \boldsymbol{S}_i \cdot \langle \boldsymbol{S}_i \rangle, \tag{15}$$

and $\langle S_i \rangle = \hat{e}_i/3$. For the fully polarized case, the system can only gain energy from the kinetic part. To gain an analytical understanding, in the weak SOC limit, by expanding the kinetic term as $e^{i\sigma\phi_{i,j}} \approx 1 + i\sigma\phi_{i,j}$, we obtain the energy difference between the FM-z and FM-x states perturbatively to the order of ϕ^2 as

$$\Delta(E_z - E_x) = \frac{\phi^2}{2N} \sum_{\boldsymbol{k},n,m} |\langle n,\boldsymbol{k}|h_{\rm soc}(\boldsymbol{k})|m,\boldsymbol{k}\rangle|^2 \times \left(\frac{n_{\rm F}(\epsilon_n) - n_{\rm F}(\epsilon_m)}{\epsilon_n - \epsilon_m} + \frac{2n_{\rm F}(\epsilon_m)}{\epsilon_n - \epsilon_m + 2U/3} \right), \tag{16}$$

with the summation of n with $|n,\boldsymbol{k}\rangle$ as the wave function of the normal state. The Fermi–Dirac distribution $n_{\rm F}$ is chosen to have $1/3$ filling. The $h_{\rm soc}(k)$ is the Fourier-transformed Hamiltonian of the SOC part and $h_{\rm soc}(k) = h^{\dagger}_{\rm soc}(k)$. We note that the first term in the bracket is always negative, while the second term is positive when U exceeds the bandwidth. Consequently, it is feasible to achieve the FM-x state, at least in the case of small U. In Fig. 5(c), we illustrate the energy difference of the lattice model Eq. (14) across varying SOC angle ϕ and Hubbard U. Our analytical results match the calculated numerical results very well. In the case of weak interaction, the SOC reduces the kinetic energy and favors the FM-x state. However, as the Hubbard U increases, the system transitions to the FM-z state. The critical value is in qualitative agreement with our HF calculation based on the continuum model. However, since the mean-field order parameter should be determined self-consistently, the critical value $U_{\rm c} \sim 20|t_1|$ is slightly overestimated.

3.2.2. FM charge density wave

Having understood the FM order, we will now examine the charge density wave. Various density waves have been identified previously.[70] When only including the nearest-neighbor V_1 term with $V_1/|t_1| \gg 1$, the particle occupancy of each kagomé triangular is limited to two. The corresponding low-energy effective model is the quantum dimer model, which has a plaquette order as the ground state.[70,73,124,125] However, this state is disrupted by the inclusion of the longer-ranged interactions V_2 and V_3, which favor a CDW state that preserves translational symmetry but polarizes the sublattices, i.e., a CDW-I state. An illustration of the different CDW states found in previous studies is shown in the insert of Fig. 5(d).[70] For our system, the V_2 and V_3 terms have similar amplitudes; therefore, we expect that the CDW-I order dominates the charge order. This is indeed what we found in our phase diagram. We notice that the phase diagram is dominated by the CDW-I state with an out-of-plane FM order whenever the CDW phase appears. Moreover, as shown in Fig. 5(b), a CDW-I state with in-plane non-colinear magnetism emerges between the FMz-CDW-I state and the FM-z state for small twisting angles. The phase transitions between different states are weakly first ordered. We also found that all the CDW states have a zero Chern number by calculating the Wilson loops of the occupied bands.

3.3. The 2/3 filling

For $2/3$ filling, the phase diagram has a much richer structure, as shown in Fig. 6(a) for twisting angle $\theta = 2^\circ$ in ϵ–$d_{\rm s}$ plane. The phase diagram in the θ–ϵ plane with the screening length $d_{\rm s} = 30$ nm is also shown in Fig. 6(b). A pinned metal droplet (PMDp) state with spin parallel to the plane emerges at the weak coupling side.[72,74] The translational symmetry is broken to an enlarged $\sqrt{3} \times \sqrt{3}$ unit cell. The structure of the PMDp state is shown in Fig. 5(c). In this state, the inner hexagonal ring has a filling of about $3/2$ and the rings are pinned by sites with opposite spin polarization. Increasing the interaction strength, when $\epsilon \sim 50$, the system transforms to a uniform charged state with a $Q = 0_1$ 120° AFM magnetic order with a gapless Dirac cone at the K point, as shown in band structure Fig. 6(c). Interestingly, this state has opposite chirality as compared with the one found in half filling. Around $\epsilon \sim 30$,

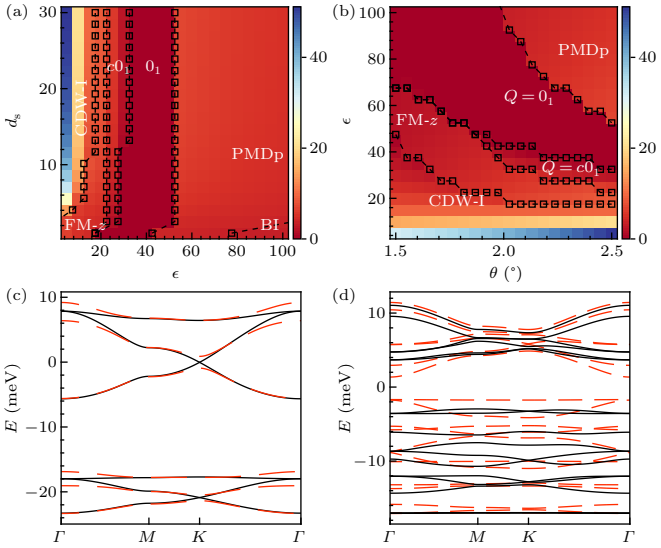


Fig. 6. [(a) and (b)] The phase diagram at $2/3$ filling in the $d_{\rm s}$–ϵ and ϵ–θ planes, respectively. The color represents the band gaps. The $Q = c0_1$ state is a canted magnetic state with 120° in plane order. BI refers to band insulator. (c) The band structure for $Q = 0_1$ (solid lines) and $Q = c0_1$ (dashed lines) states at $\theta = 2^\circ$, $d_{\rm s} = 30$ nm and $\epsilon = 40$. (d) The band structure for in-plane (solid lines) and out-of-plane (dashed lines) pinned metal droplet states $\theta = 2.5^\circ$, $d_{\rm s} = 30$ nm and $\epsilon = 60$. It can be observed that the in-plane state possesses a larger band gap, which reduces the energy in comparison to the out-of-plane case.

the system becomes gapped with non-zero out-of-plane magnetization and a non-zero Chern number as the interaction is further increased. However, the in-plane spin order is the same as the $Q = 0_1$ state. The system lowers its kinetic energy by developing gaps in the band structure. The band topology originates from the non-zero spin chirality. The band structure of those states are shown in Figs. 6(c) and 6(d) for typical parameters. Interestingly, the quasi-particle flat band manifests at the top for $Q = 0_1$ states. This is in a notable contrast to the single-particle case. Further increasing the interaction strength, the system transits to an FM-z state and a CDW state, similar to the $1/3$ filling case at stronger interaction. The CDW state is a particle–hole partner to the $1/3$ filling case. We notice that the overall phase diagram is consistent with a previous study on a lattice model with only Hubbard interaction and the SOC.[74]

4. Discussion and conclusion

Based on the HF mean field theory, we calculated the phase diagram for a twisted bilayer PdS_2 with kagomé band structure at rational filling $1/2$, $1/3$ and $2/3$. At half filling, we found that the spin–orbit coupling stabilizes the $Q = 0_2$ state with 120° magnetic order. There is a phase transition to the out-of-plane FM ordered state due to the direct exchange interaction. At $1/3$ filling, the frustrated nature of the lattice structure favors the FM state. We emphasize that an FM correlation with a similar mechanism has been experimentally observed in moiré heterostructures, such as WSe_2/WS_2, and cold atom quantum simulators with triangular lattices.[17,122] Our kagomé lattice system provides a complementary approach to this kinetic magnetism. It would also be interesting to study the spin polarons in the future.[126–130] For $2/3$ filling, the in-plane PMD state, 120° AFM semi-metal and canted 120° order were identified besides the FM-z state, which is consistent with a previous study on the kagomé-Hubbard model with strong SOC.[74] Within the fully polarized FM state, CDW states with sublattice polarization were found. We notice for the twisting angle we studied, when bands are isolated from remote bands, the single-particle part is well described by nearest hopping. Therefore, the correlated ordered state found in this system is insensitive to the twisting angle. Our system provides a platform for exploring the correlation physics in kagomé lattices.

Finally, we would like to discuss possible future directions. On the material side, our system has strong spin–orbit coupling, which breaks the spin $SU(2)$ symmetry; thus a magnetically ordered state is stabilized at half filling. Therefore, it would be interesting to find materials with a degenerate Γ valley with weak spin–orbit coupling such that one may realize an $SU(2)$ symmetric kagomé Hubbard model near the charge neutral point. Exotic phases such as spin liquids could be expected. On the other hand, the phase diagrams were identified using the HF method, which is known to underestimate the role of quantum fluctuation.[131] The kagomé lattice Hubbard model or t–J model has been extensively explored in the literature, but mostly concentrating on the $SU(2)$ symmetric system.[65,95–101] More sophisticated methods may be included to study this model with strong SOC and long-range Coulomb interaction.[47] Moreover, we have restricted the HF calculation to certain ansatzes. Therefore, more exotic magnetic and charge orders, such as spin spiral order and charge stripes, may be found by relaxing this constraint.[37,132] Also, when the Chern band is fractionally filled, the FM state is stabilized in a small ϵ limit by direct exchange interaction. This raises the possibility of realizing a fractional Chern insulator with a long-range Coulomb interaction.[133–135] We leave all these intriguing questions for future research.

Acknowledgments

Project supported by the National Natural Science Foundation of China (Grant Nos. 12350404 and 12174066), the Innovation Program for Quantum Science and Technology (Grant No. 2021ZD0302600), the National Key Research and Development Program of China (Grant No. 2019YFA0308404), and the Science and Technology Commission of Shanghai Municipality (Grant Nos. 23JC1400600 and 2019SHZDZX01).

References

[1] Carr S, Fang S and Kaxiras E 2020 *Nat. Rev. Mater.* **5** 748
[2] Andrei E Y and MacDonald A H 2020 *Nat. Mater.* **19** 1265
[3] Kennes D M, Claassen M, Xian L, Georges A, Millis A J, Hone J, Dean C R, Basov D, Pasupathy A N and Rubio A 2021 *Nat. Phys.* **17** 155
[4] Andrei E Y, Efetov D K, Jarillo-Herrero P, MacDonald A H, Mak K F, Senthil T, Tutuc E, Yazdani A and Young A F 2021 *Nat. Rev. Mater.* **6** 201
[5] Mak K F and Shan J 2022 *Nat. Nanotechnol.* **17** 686
[6] Cao Y, Fatemi V, Demir A, Fang S, Tomarken S L, Luo J Y, Sanchez-Yamagishi J D, Watanabe K, Taniguchi T, Kaxiras E, Ashoori R C and Jarillo-Herrero P 2018 *Nature* **556** 80
[7] Cao Y, Fatemi V, Fang S, Watanabe K, Taniguchi T, Kaxiras E and Jarillo-Herrero P 2018 *Nature* **556** 43
[8] Bistritzer R and MacDonald A H 2011 *Proc. Natl. Acad. Sci. USA* **108** 12233
[9] Sharpe A L, Fox E J, Barnard A W, Finney J, Watanabe K, Taniguchi T, Kastner M and Goldhaber-Gordon D 2019 *Science* **365** 605
[10] Lu X, Stepanov P, Yang W, Xie M, Aamir M A, Das I, Urgell C, Watanabe K, Taniguchi T, Zhang G, Bachtold A, MacDonald A H and Efetov D K 2019 *Nature* **574** 653
[11] Serlin M, Tschirhart C L, Polshyn H, Zhang Y, Zhu J, Watanabe K, Taniguchi T, Balents L and Young A F 2020 *Science* **367** 900
[12] Nuckolls K P, Oh M, Wong D, Lian B, Watanabe K, Taniguchi T, Bernevig B A and Yazdani A 2020 *Nature* **588** 610
[13] Xie Y, Pierce A T, Park J M, Parker D E, Khalaf E, Ledwith P, Cao Y, Lee S H, Chen S, Forrester P R, Watanabe K, Taniguchi T, Vishwanath A, Jarillo-Herrero P and Yacoby A 2021 *Nature* **600** 439
[14] Wang L, Shih E M, Ghiotto A, Xian L, Rhodes D A, Tan C, Claassen M, Kennes D M, Bai Y, Kim B, Watanabe K, Taniguchi T, Zhu X, Hone J, Rubio A, Pasupathy A N and Dean C R 2020 *Nat. Mater.* **19** 861
[15] Tang Y, Li L, Li T, Xu Y, Liu S, Barmak K, Watanabe K, Taniguchi T, MacDonald A H, Shan J and Mak K F 2020 *Nature* **579** 353

[16] Regan E C, Wang D, Jin C, Utama M I B, Gao B, Wei X, Zhao S, Zhao W, Zhang Z, Yumigeta K, Blei M, Carlström J D, Watanabe K, Taniguchi T, Tongay S, Crommie M, Zettl A and Wang F 2020 *Nature* **579** 359
[17] Xu Y, Liu S, Rhodes D A, Watanabe K, Taniguchi T, Hone J, Elser V, Mak K F and Shan J 2020 *Nature* **587** 214
[18] Li T, Jiang S, Shen B, Zhang Y, Li L, Tao Z, Devakul T, Watanabe K, Taniguchi T, Fu L, Shan J and Mak K F 2021 *Nature* **600** 641
[19] Li T, Jiang S, Li L, Zhang Y, Kang K, Zhu J, Watanabe K, Taniguchi T, Chowdhury D, Fu L, Shan J and Mak K F 2021 *Nature* **597** 350
[20] Ghiotto A, Shih E M, Pereira G S, Rhodes D A, Kim B, Zang J, Millis A J, Watanabe K, Taniguchi T, Hone J C, Wang L, Dean C R and Pasupathy A N 2021 *Nature* **597** 345
[21] Li H, Li S, Regan E C, Wang D, Zhao W, Kahn S, Yumigeta K, Blei M, Taniguchi T, Watanabe K, Tongay S, Zettl A, Crommie M F and Wang F 2021 *Nature* **597** 650
[22] Tang Y, Gu J, Liu S, Watanabe K, Taniguchi T, Hone J C, Mak K F and Shan J 2022 *Nat. Commun.* **13** 4271
[23] Wang P, Yu G, Kwan Y H, Jia Y, Lei S, Klemenz S, Cevallos F A, Singha R, Devakul T, Watanabe K, Taniguchi T, Sondhi S L, Cava R J, Schoop L M, Parameswaran S A and Wu S 2022 *Nature* **605** 57
[24] Zhao W, Shen B, Tao Z, Han Z, Kang K, Watanabe K, Taniguchi T, Mak K F and Shan J 2023 *Nature* **616** 61
[25] Cai J, Anderson E, Wang C, Zhang X, Liu X, Holtzmann W, Zhang Y, Fan F, Taniguchi T, Watanabe K, Ran Y, Cao T, Fu L, Xiao D, Yao W and Xu X 2023 *Nature* **622** 63
[26] Zeng Y, Xia Z, Kang K, Zhu J, Knüppel P, Vaswani C, Watanabe K, Taniguchi T, Mak K F and Shan J 2023 *Nature* **622** 69
[27] Yu G, Wang P, Uzan-Narovlansky A J, Jia Y, Onyszczak M, Singha R, Gui X, Song T, Tang Y, Watanabe K, *et al.* 2023 *Nat. Commun.* **14** 7025
[28] Park H, Cai J, Anderson E, Zhang Y, Zhu J, Liu X, Wang C, Holtzmann W, Hu C, Liu Z, Taniguchi T, Watanabe K, haw Chu J, Cao T, Fu L, Yao W, Chang C Z, Cobden D, Xiao D and Xu X 2023 *Nature* **622** 74
[29] Xu F, Sun Z, Jia T, Liu C, Xu C, Li C, Gu Y, Watanabe K, Taniguchi T, Tong B, Jia J, Shi Z, Jiang S, Zhang Y, Liu X and Li T 2023 *Phys. Rev. X* **13** 031037
[30] Wu F, Lovorn T, Tutuc E, Martin I and MacDonald A H 2019 *Phys. Rev. Lett.* **122** 086402
[31] Naik M H and Jain M 2018 *Phys. Rev. Lett.* **121** 266401
[32] Zhang Y, Liu T and Fu L 2021 *Phys. Rev. B* **103** 155142
[33] Angeli M and MacDonald A H 2021 *Proc. Natl. Acad. Sci. USA* **118** e2021826118
[34] Zhang Y, Yuan N F Q and Fu L 2020 *Phys. Rev. B* **102** 201115
[35] Xian L, Claassen M, Kiese D, Scherer M M, Trebst S, Kennes D M and Rubio A 2021 *Nat. Commun.* **12** 5644
[36] Wu F, Lovorn T, Tutuc E and MacDonald A H 2018 *Phys. Rev. Lett.* **121** 026402
[37] Pan H, Wu F and Das Sarma S 2020 *Phys. Rev. B* **102** 201104
[38] Pan H, Wu F and Das Sarma S 2020 *Phys. Rev. Res.* **2** 033087
[39] Morales-Durán N, Hu N C, Potasz P and MacDonald A H 2022 *Phys. Rev. Lett.* **128** 217202
[40] Hu N C and MacDonald A H 2021 *Phys. Rev. B* **104** 214403
[41] Crépel V and Fu L 2023 *Phys. Rev. B* **107** L201109
[42] Reddy A P, Devakul T and Fu L 2023 *Phys. Rev. Lett.* **131** 246501
[43] Wang C, Zhang X W, Liu X, He Y, Xu X, Ran Y, Cao T and Xiao D 2024 *Phys. Rev. Lett.* **132** 036501
[44] Qiu W X, Li B, Luo X J and Wu F 2023 *Phys. Rev. X* **13** 041026
[45] Kaushal N and Dagotto E 2023 *Phys. Rev. B* **107** L201118
[46] Goldman H, Reddy A P, Paul N and Fu L 2023 *Phys. Rev. Lett.* **131** 136501
[47] Song Z, Seifert U F P, Luo Z X and Balents L 2023 *Phys. Rev. B* **108** 155109
[48] Reddy A P, Alsallom F, Zhang Y, Devakul T and Fu L 2023 *Phys. Rev. B* **108** 085117
[49] Motruk J, Rossi D, Abanin D A and Rademaker L 2023 *Phys. Rev. Res.* **5** L022049
[50] Han J, Lai K, Yu X, Chen J, Guo H and Dai J 2023 *Chin. Phys. Lett.* **40** 067801
[51] Wang R and Song Z 2024 *Chin. Phys. Lett.* **41** 047101
[52] Zhou X and Shen J 2024 *Chin. Phys. Lett.* **41** 047403
[53] Liu Z, Wang H and Wang J 2022 *Phys. Rev. B* **106** 035114
[54] Wang H, Jiang Y, Liu Z and Wang J 2022 arXiv:2209.06524 [cond-mat.mes-hall]
[55] Claassen M, Xian L, Kennes D M and Rubio A 2022 *Nat. Commun.* **13** 4915
[56] Scheer M G and Lian B 2023 *Phys. Rev. B* **108** 245136
[57] Scheer M G and Lian B 2023 *Phys. Rev. Lett.* **131** 266501
[58] Ramirez A P 1994 *Ann. Rev. Mater. Sci.* **24** 453
[59] Balents L 2010 *Nature* **464** 199
[60] Kita T, Ohashi T and Kawakami N 2013 *Phys. Rev. B* **87** 155119
[61] Guertler S 2014 *Phys. Rev. B* **90** 081105
[62] Higa R and Asano K 2016 *Phys. Rev. B* **93** 245123
[63] Sun R Y and Zhu Z 2021 *Phys. Rev. B* **104** L121118
[64] Mielke A 1992 *J. Phys. A Math. Gen.* **25** 4335
[65] Koretsune T and Ogata M 2003 *J. Phys. Soc. Jpn.* **72** 2437
[66] Hanisch T, Kleine B, Ritzl A and Müller-Hartmann E 1995 *Ann. Phys.* **507** 303
[67] Tanaka A and Ueda H 2003 *Phys. Rev. Lett.* **90** 067204
[68] Pollmann F, Fulde P and Shtengel K 2008 *Phys. Rev. Lett.* **100** 136404
[69] Liu Q, Yao H and Ma T 2010 *Phys. Rev. B* **82** 045102
[70] Wen J, Rüegg A, Wang C C J and Fiete G A 2010 *Phys. Rev. B* **82** 075125
[71] Nishimoto S, Nakamura M, O'Brien A and Fulde P 2010 *Phys. Rev. Lett.* **104** 196401
[72] Ferhat K and Ralko A 2014 *Phys. Rev. B* **89** 155141
[73] Pollmann F, Roychowdhury K, Hotta C and Penc K 2014 *Phys. Rev. B* **90** 035118
[74] Kim H S, Mishra A and Lee S 2020 *Phys. Rev. B* **102** 155113
[75] Ferrari F, Becca F and Valentí R 2022 *Phys. Rev. B* **106** L081107
[76] Guo H M and Franz M 2009 *Phys. Rev. B* **80** 113102
[77] Ren Y, Zeng T S, Zhu W and Sheng D N 2018 *Phys. Rev. B* **98** 205146
[78] Ren Y, Jiang H C, Qiao Z and Sheng D 2021 *Phys. Rev. Lett.* **126** 117602
[79] Kiesel M L and Thomale R 2012 *Phys. Rev. B* **86** 121105
[80] Kiesel M L, Platt C and Thomale R 2013 *Phys. Rev. Lett.* **110** 126405
[81] Wang W S, Li Z Z, Xiang Y Y and Wang Q H 2013 *Phys. Rev. B* **87** 115135
[82] Wang W S, Liu Y C, Xiang Y Y and Wang Q H 2016 *Phys. Rev. B* **94** 014508
[83] Schwemmer T, Hohmann H, Dürrnagel M, Potten J, Beyer J, Rachel S, Wu Y M, Raghu S, Müller T, Hanke W and Thomale R 2024 *Phys. Rev. B* **110** 024501
[84] Elser V 1989 *Phys. Rev. Lett.* **62** 2405
[85] Marston J B and Zeng C 1991 *J. Appl. Phys.* **69** 5962
[86] Sachdev S 1992 *Phys. Rev. B* **45** 12377
[87] Wang F and Vishwanath A 2006 *Phys. Rev. B* **74** 174423
[88] Ran Y, Hermele M, Lee P A and Wen X G 2007 *Phys. Rev. Lett.* **98** 117205
[89] Yan S, Huse D A and White S R 2011 *Science* **332** 1173
[90] Depenbrock S, McCulloch I P and Schollwöck U 2012 *Phys. Rev. Lett.* **109** 067201
[91] Cépas O, Fong C M, Leung P W and Lhuillier C 2008 *Phys. Rev. B* **78** 140405
[92] Messio L, Cépas O and Lhuillier C 2010 *Phys. Rev. B* **81** 064428
[93] Huh Y, Fritz L and Sachdev S 2010 *Phys. Rev. B* **81** 144432
[94] Messio L, Lhuillier C and Misguich G 2011 *Phys. Rev. B* **83** 184401
[95] Indergand M, Läuchli A, Capponi S and Sigrist M 2006 *Phys. Rev. B* **74** 064429
[96] Ko W H, Lee P A and Wen X G 2009 *Phys. Rev. B* **79** 214502
[97] Guertler S and Monien H 2011 *Phys. Rev. B* **84** 174409
[98] Guertler S and Monien H 2013 *Phys. Rev. Lett.* **111** 097204
[99] Jiang H C, Devereaux T and Kivelson S 2017 *Phys. Rev. Lett.* **119** 067002
[100] Peng C, Jiang Y F, Sheng D N and Jiang H C 2021 *Adv. Quantum Technol.* **4** 2000126
[101] Jiang Y F, Yao H and Yang F 2021 *Phys. Rev. Lett.* **127** 187003
[102] Damle A, Lin L and Ying L 2015 *J. Chem. Theory Comput.* **11** 1463
[103] Damle A and Lin L 2018 *Multiscale Model. Simul.* **16** 1392
[104] Damle A, Levitt A and Lin L 2019 *Multiscale Model. Simul.* **17** 167
[105] Marzari N and Vanderbilt D 1997 *Phys. Rev. B* **56** 12847
[106] Kang J and Vafek O 2018 *Phys. Rev. X* **8** 031088
[107] Koshino M, Yuan N F, Koretsune T, Ochi M, Kuroki K and Fu L 2018 *Phys. Rev. X* **8** 031087

[108] Luo X J, Wang M and Wu F 2023 *Phys. Rev. B* **107** 235127

[109] Xu C, Li J, Xu Y, Bi Z and Zhang Y 2024 *Proc. Natl. Acad. Sci. USA* **121** e2316749121

[110] Vitale V, Pizzi G, Marrazzo A, Yates J R, Marzari N and Mostofi A A 2020 *npj Comput. Mater.* **6** 66

[111] Bultinck N, Khalaf E, Liu S, Chatterjee S, Vishwanath A and Zaletel M P 2020 *Phys. Rev. X* **10** 031034

[112] Bernevig B A, Song Z D, Regnault N and Lian B 2021 *Phys. Rev. B* **103** 205413

[113] Xie F, Kang J, Bernevig B A, Vafek O and Regnault N 2023 *Phys. Rev. B* **107** 075156

[114] Kudin K N, Scuseria G E and Cancès E 2002 *J. Chem. Phys.* **116** 8255

[115] Garza A J and Scuseria G E 2012 *J. Chem. Phys.* **137** 054110

[116] MacDonald A H, Girvin S M and Yoshioka D 1988 *Phys. Rev. B* **37** 9753

[117] Nagaoka Y 1966 *Phys. Rev.* **147** 392

[118] Tasaki H 1989 *Phys. Rev. B* **40** 9192

[119] Ciorciaro L, Smoleński T, Morera I, Kiper N, Hiestand S, Kroner M, Zhang Y, Watanabe K, Taniguchi T, Demler E, *et al.* 2023 *Nature* **623** 509

[120] Morera I, Kanász-Nagy M, Smolenski T, Ciorciaro L, Imamoğlu A and Demler E 2023 *Phys. Rev. Res.* **5** L022048

[121] Lee K, Sharma P, Vafek O and Changlani H J 2023 *Phys. Rev. B* **107** 235105

[122] Xu M, Kendrick L H, Kale A, Gang Y, Ji G, Scalettar R T, Lebrat M and Greiner M 2023 *Nature* **620** 971

[123] Li C, He M G, Wang C Y and Zhai H 2024 *Phys. Rev. B* **109** 165131

[124] Moessner R, Sondhi S L and Chandra P 2001 *Phys. Rev. B* **64** 144416

[125] O'Brien A, Pollmann F and Fulde P 2010 *Phys. Rev. B* **81** 235115

[126] van de Kraats J, Nielsen K K and Bruun G M 2022 *Phys. Rev. B* **106** 235143

[127] Seifert U F P and Balents L 2024 *Phys. Rev. Lett.* **132** 046501

[128] Zhang Y and Fu L 2023 *SciPost Phys. Core* **6** 038

[129] Davydova M, Zhang Y and Fu L 2023 *Phys. Rev. B* **107** 224420

[130] Tao Z, Zhao W, Shen B, Knüppel P, Watanabe K, Taniguchi T, Shan J and Mak K F 2023 arXiv:2307.12205 [cond-mat.str-el]

[131] Yang Y, Morales M A and Zhang S 2024 *Phys. Rev. Lett.* **132** 076503

[132] Kaushal N, Morales-Durán N, MacDonald A H and Dagotto E 2022 *Commun. Phys.* **5** 289

[133] Tang E, Mei J W and Wen X G 2011 *Phys. Rev. Lett.* **106** 236802

[134] Sun K, Gu Z, Katsura H and Das Sarma S 2011 *Phys. Rev. Lett.* **106** 236803

[135] Neupert T, Santos L, Chamon C and Mudry C 2011 *Phys. Rev. Lett.* **106** 236804